Contrib Mineral Petrol (2006) 151: 651–664
DOI 10.1007/s00410-006-0082-7

ORIGINAL PAPER

Kevin J. Grant · Simon C. Kohn · Richard A. Brooker

# Solubility and partitioning of water in synthetic forsterite and enstatite in the system $MgO–SiO_2–H_2O±Al_2O_3$

Received: 10 August 2005 / Accepted: 22 February 2006 / Published online: 19 April 2006


**Abstract** The solubility of water in coexisting enstatite and forsterite was investigated by simultaneously synthesizing the two phases in a series of high pressure and temperature piston cylinder experiments. Experiments were performed at 1.0 and 2.0 GPa at temperatures between 1,100 and 1,420°C. Integrated OH absorbances were determined using polarized infrared spectroscopy on orientated single crystals of each phase. Phase water contents were estimated using the calibration of Libowitzky and Rossman (Am Mineral 82:1111–1115, 1997). Enstatite crystals, synthesized in equilibrium with forsterite and an aqueous phase at 1,350°C and 2.0 GPa, contain 114 ppm $H_2O$. This is reduced to 59 ppm at 1,100°C, under otherwise identical conditions, suggesting a strong temperature dependence. At 1,350°C and 1.0 GPa water solubility in enstatite is 89 ppm, significantly lower than that at 2.0 GPa. In contrast water solubility in forsterite is essentially constant, being in the range 36–41 ppm for all conditions studied. These data give partition coefficients $D_{H_2O}^{en/fo}$ in the range 2.28–3.31 for all experiments at 1,350°C and 1.34 for one experiment at 1,100°C. The incorporation of $Al_2O_3$ in enstatite modifies the OH stretching spectrum in a systematic way, and slightly increases the water solubility.

Communicated by J. Hoefs

K. J. Grant (✉) · S. C. Kohn · R. A. Brooker
Department of Earth Sciences, University of Bristol,
Wills Memorial Building,
Queens Road, BS8 1RJ Bristol, UK
E-mail: kgrant@els.mq.edu.au
Tel.: +44-117-3315002
Fax: +44-117-9253385

*Present address*: K. J. Grant
Department of Earth and Planetary Sciences,
Macquarie University, 2109 Sydney, NSW, Australia

*Present address*: R. A. Brooker
Department of Earth Sciences, University College London,
Gower Street, London WC1E 6BT, UK
E-mail: richard.brooker@ucl.ac.uk

## Introduction

Accurate partition coefficients that describe the distribution of elements between minerals and melts are pivotal to understanding fractionation in magmatic processes. Relatively small amounts of water can have a profound influence on the physiochemical parameters of rocks, minerals, and melts. Water solubility in individual mantle phases has been the focus of significant research [reviewed in Ingrin and Skogby (2000); Libowitzky and Beran (2004)] but systematic studies into the partitioning between coexisting phases remain sparse. Studies of water solubility in mantle xenoliths may provide some information about water partitioning in the natural environment (Peslier et al. 2002; Bell et al. 2004) but application of the data they yield to the source region has been questioned because of rapid hydrogen diffusion through NAMs at high temperatures (Mackwell and Kohlstedt 1990). Experimental methods provide an opportunity to reproduce pressure and temperature conditions prevailing in the mantle. Synthetic samples can be rapidly quenched and so direct measurement of equilibrium distribution of water between mantle silicates can be made.

In this paper we will present the results of a series of experiments designed to provide information on the relative solubility of water in olivine and orthopyroxene, the two most volumetrically important silicate phases in the Earth's upper mantle. The experiments were performed in the system $MgO–SiO_2–H_2O$, the simplest system in which olivine and enstatite are stable together over a wide range of pressure and temperature. In addition some samples were synthesized with small but significant quantities of $Al_2O_3$. A relatively simple starting chemistry limits the influence of additional complicating factors associated with complex evolving crystal chemistries during a crystallization experiment. Thus, our data can be considered to be a point of reference against which data in more complex systems can be compared. The data also place constraints upon the

effect of pressure, temperature and chemical environment on the distribution of water between these phases and permit us to place some constraints on the effect of such changes in the upper mantle.

## Experimental procedures

### Starting materials

Crystals of olivine and orthopyroxene were synthesized from starting materials prepared by mixing powders of reagent grade oxides and specpure $MgOH_2$ (brucite) (Supplied by Intermag Co. Ltd). Electron microprobe analyses of glass prepared from the starting materials used in the experiments suggests that the composition is equivalent to enstatite plus a few percent of excess $SiO_2$. The initial water content of each run varied between 4.5 and 18 wt% and was controlled by incorporating the different ratios of $Mg(OH)_2$ and MgO in the starting mixture. Although the compositions were intended to be pure $MgO–SiO_2–H_2O$, small but significant impurities were accidentally introduced and these will be shown to have important effects on the incorporation of $H_2O$.

### High-pressure experiments

Crystals were synthesized at high pressure and temperature in an end loaded, 3/4 in. diameter piston cylinder [See McDade et al. (2002) for details of the experimental setup used]. Starting materials were packed into 6 mm diameter platinum capsules and welded shut. The sealed capsules were placed in crushable alumina sleeves and loaded into 0.75 in. talc-pyrex assemblies. Temperatures were measured using W-Re thermocouples located at the top of the sample capsule. A tapered graphite furnace temperature was used to reduce thermal gradients across the sample cell (±10°C). No pressure correction was applied as these cells have been shown to reproduce the nominal pressure to within 4% (McDade et al. 2002). Capsules were checked for leaks both before and after experiments.

### Crystal synthesis

Crystal growth was initiated and controlled by synthesis under three different thermal regimes. Most of the experiments were conducted isothermally; samples were heated to the required temperature and held there for the duration of the run. Samples EN12 and EN13 were initially heated to 1,420°C and then steadily cooled at 2°C/h to 1,350°C. Each run was then held at 1,350°C for 41 h before being quenched. Sample EN9 was heated to 1,420°C, held at this temperature for 1 h, cooled rapidly (1,000°C/h) to 1,350°C and then held at this temperature for 60 h. All samples were quenched by switching off power to the furnace. All experiments were performed at pressures and temperatures well outside the amphibole stability field (Rauch and Keppler 2002).

### Sample preparation and phase identification

After each experiment the capsule was carefully opened into an agate mortar and left to dry. The run products were examined optically and with a Hitachi S3500 N scanning electron microscope. The phases identified are described on Table 1. A large number of separate clear and euhedral olivine and enstatite crystals were hand-picked from the dried capsule contents. Individual crystals (ranging in diameter from 200 μm to 5 mm) were set in resin using their morphology to ensure that the horizontal plane was parallel to one of the faces, and hence also to one of the crystallographic axes.

**Table 1** Experimental conditions used in synthesis of samples, and the phases identified in the run products

| | *P* (GPa) | *T* (start) | *T* (end) | Cool rate (°C/h) | Total run duration (h) | $H_2O$[a] (%) | Run products identified |
|---|---|---|---|---|---|---|---|
| EN1 | 2.0 | 1350 | 1350 | NA | 61 | 9 | Fo/En/fl |
| EN2 | 1.0 | 1350 | 1350 | NA | 109 | 9 | Fo/En/fl |
| EN3 | 1.0 | 1420 | 1420 | NA | 64 | 9 | En/m |
| EN4 | 2.0 | 1350 | 1350 | NA | 69 | 9 | Fo/En/fl |
| EN5 | 2.0 | 1350 | 1350 | NA | 65 | 18 | Fo/En/fl |
| EN6 | 2.0 | 1100 | 1100 | NA | 44 | 9 | Fo/En/fl |
| EN7[b] | 2.0 | 1350 | 1350 | NA | 61 | 9 | Fo/En/fl |
| EN8 | 2.0 | 1350 | 1350 | NA | 61 | 4.5 | Fo/En/fl |
| EN9[c] | 2.0 | 1420 | 1350 | 1,000 | 61 | 9 | En/fl |
| EN11[d] | 2.0 | 1350 | 1350 | NA | 41 | 9 | En/fl |
| EN12 | 2.0 | 1420 | 1350 | 2 | 76 | 9 | Fo/En/fl |
| EN13[d] | 2.0 | 1420 | 1350 | 2 | 76 | 9 | En/fl |

*Fo* forsterite, *En* enstatite, *m* silicate melt quenched to an interlocking mass of skeletal enstatite crystals, *fl* dendrites and spheres of $SiO_2$ which represent the products of quenching an aqueous fluid

[a] Nominal $H_2O$ contents in starting mixture

[b] Starting material contained an extra 5 wt% MgO

[c] Run was heated to 1,480°C, held for 1 h, then cooled at 1,000°C/h to 1,350°C and held for 60 h

[d] Starting material contained an extra 1 wt% $Al_2O_3$

The crystals were then carefully ground on both sides and double polished down to a thickness of 50–150 μm for FTIR measurements. The thickness of the finished sample wafers was measured with an accuracy of ±1 μm using a digital micrometer. Phase chemistries were determined, wherever possible on the same crystals as prepared for infrared analysis, with a Jeol JXA 8600 superprobe at the University of Bristol using an accelerating voltage of 15 kV and a sample current of 10 nA. Count times of 20 s were used to measure all elements. Mg, Si and Al were discovered in the synthetic phases. Na, Ti, Ca, Mn and Fe were below detection limit in every analysis performed.

## Infrared spectroscopy

Polarized infrared absorbance spectra were recorded between 650 and 5,500 $cm^{-1}$ using a NicPlan infrared microscope and a Nicolet Nexus FTIR spectrometer. A globar™ source and KBr beamsplitter were housed in the Nicolet bench. A dedicated MCT detector and Spectra-Tech Zn Se polarizer are located in the microscope. Sample wafers were placed on a KBr disc on the microscope stage and measured through a 200 μm diameter circular aperture located in the microscope unit. Infrared absorbance spectra were collected with the electric field vector of the infrared radiation parallel to each of the optical indexes of the crystals. Crystallographic orientation of each polarized spectrum was confirmed using the overtone and combination modes between 2,350 and 1,250 $cm^{-1}$ (Grant and Brooker, in preparation). In that study Grant and Brooker (in preparation) collected polarized infrared spectra on natural and synthetic olivine and orthopyroxene crystals. These had been previously oriented using well-defined crystallographic faces and single crystals XRD analyses. Polarized infrared absorbance spectra were then collected on a selection of double-polished olivine or orthopyroxene crystals. Polarized spectra were measured at 10° increments by turning the sample on the rotating sample stage. Using the polarized absorbance spectrum measured parallel to each crystallographic axis on the original oriented samples as a template, spectra collected parallel to each crystallographic orientation could be identified. Experiments which aimed to ascertain the degree of accuracy afforded through employing this method is dependant upon sample chemistry, at close to end member compositions samples can be aligned to within 5° of that attained using single crystal XRD.

For each infrared analysis performed in this study, sample and background spectra were collected by accumulating 512 scans obtained at a resolution of 4 $cm^{-1}$. The background spectrum was collected immediately after the sample spectrum, with the polarizer aligned in the same orientation. The entire infrared microscope unit is held within a Perspex (PMMA) box and both the microscope and spectrometer are continuously purged with dry air to remove fluctuations in the atmospheric water concentration. Infrared spectra were measured only after the crystals had been sealed in the microscope for at least 12 h.

## Quantifying OH defect concentrations

All spectra were normalized to a 1 cm optical path length so that the spectra for samples of different thickness could be compared directly. The normalized thickness of each polarized spectrum was also checked for intra-sample consistency by correlating the intensity of overtone and/or combination vibrations in the region 2,400–1,200 $cm^{-1}$ (Grant and Brooker, in preparation). These bands were also used to check crystal orientation, which was usually within 5° of the stated crystallographic axis.

Accurately subtracting a baseline from a raw infrared spectrum is recognized as one of the most problematic aspects faced when using infrared spectroscopy to quantify OH in minerals (Bell et al. 1995; Bell et al. 2003; Koga et al. 2003). Constraining the background as accurately as possible formed a significant part of this study. As several approaches to defining the background were used these are described here in some detail along with relative merits and disadvantages of each. In the following descriptions polarized spectra measured along each crystallographic direction were treated separately. Spectra of olivine and orthopyroxene were initially fitted with a linear baseline between 3,900 and 2,500 $cm^{-1}$. Theoretically this approach is justified for iron-free samples, as the OH stretching region should be superimposed upon a flat background. This approach provided an appropriate solution when subtracting a background from near end-member forsterite. However, in enstatite sharp OH bands are superimposed upon a broad absorption feature and in practice fitting a background to regions of the spectrum immediately adjacent to the OH stretching bands was rarely satisfactorily achieved using this technique. We therefore fitted a background to enstatite spectra using a polynomial function between 4,000 and 2,500 $cm^{-1}$ (Fig. 1a). This second technique generated a more realistic background to the sample spectrum. It is worth noting here that the integrated OH absorbance calculated from a spectrum derived by this method may be considerably less than that estimated using a linear background.

Our original intention was to fit individual OH peaks from the background subtracted spectrum (see Fig. 1b) using the PeakFit computer program (Jandel Scientific). However we noted that peak fitting the background subtracted spectrum frequently led to a poor correlation between the integrated absorbencies of corresponding bands resolved on different spectra from the same sample. By superimposing assorted spectra from the same sample measured along the same crystallographic direction it became clear that although the heights of individual OH bands in a sample (defined as absorbance maxima relative to the adjacent minima) were almost

identical, the overall integrated absorbance of different spectra may vary markedly (Fig. 2). Subtracting a spectrum with a large total integrated OH absorbance from that of a sample with a low value, one is left with a residual broad absorbance feature centered at approximately 3,250 $cm^{-1}$. A similar feature is identified when individual peaks observed in the spectrum are resolved into component bands using the PeakFit computer program (Fig. 1b). A crystal measured through the same point twice but with the polarizer rotated perpendicularly generates two spectra which, once resolved into individual peaks, both contain a broad absorbance of similar magnitude. However, this isotropic absorption varies markedly in intensity between different crystals from the same experiment. Although the regions selected for analysis were carefully selected to be free of inclusions and fractures, the most likely origin for this band is molecular water in the beam path. The isotropic nature and variability from crystal to crystal suggest that this molecular water component is not incorporated within the crystal structure and is does not represent part of the equilibrium water solubility. Therefore the water contents reported here represent those estimated from the integrated sum of band intensities resolved using PeakFit, but exclude the broad 3,250 $cm^{-1}$ component. Polarized spectra from which quantitative measurements were made were averaged across several crystals from each experiment, measured parallel to each crystallographic direction. OH peaks recorded on each averaged spectrum were resolved into separate bands using PeakFit. The integrated absorbance and an integrated absorption coefficient were then calculated for each resolved band using the Beer-Lambert Law and the empirical calibration of Libowitzky and Rossman (1997). Although the infrared bands correspond to the vibrations of OH species, and these OH groups may be isolated OH, clustered groups such as in the hydrogarnet substitution or even $H_2O$ molecules, all the solubility data reported in this paper is expressed as wt ppm $H_2O$. This is the formalism used in the majority of previous papers, but care must be taken in comparing data from the literature as some is expressed as wt ppm OH, molar H/Si ratio etc. The $H_2O$ contents corresponding to each band were then summed to generate an $H_2O$ content representative of each direction. The total $H_2O$ content of a sample was then obtained by summing the $H_2O$ contents of each of the three crystallographic directions.

Libowitzky and Rossman (1997) describe a technique for calculating the molar absorption coefficient of an

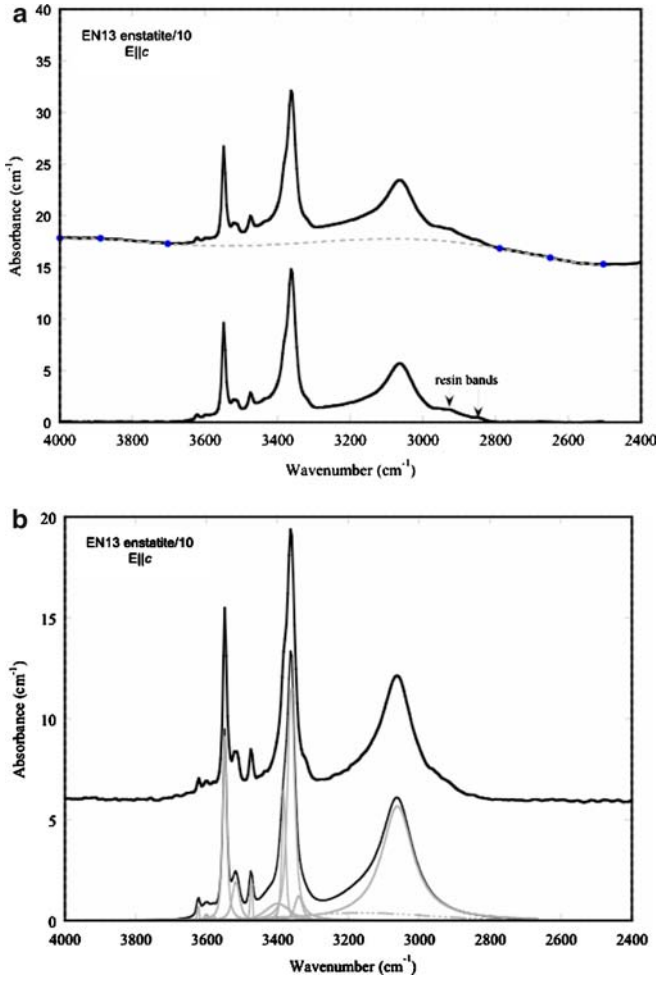


**Fig. 1** **a** Representative polarized infrared spectra of enstatite measured where E || *c* in selected crystals from sample EN13 the region 4,000–2,600 $cm^{-1}$. The *dashed line* is the background which is subtracted (see text for explanation), and the lower curve is the background subtracted spectrum. **b** Fitting of an experimental spectrum (*thick black line*) measured E || *c* in sample EN13. The spectrum is fitted with 13 individual bands (*light gray*) which sum to give the spectrum shown in the *thin black line*. The broad band (*dashed gray*) represents a broad absorption necessary to accurately replicate the original. The normalized intensity of any individual sharp band is constant in spectra from the same sample, but the intensity of this anistropic, broad band varies. We interpret this band to be caused by non-defect water in the sample and excluded this component when calculating the total water budget of the sample

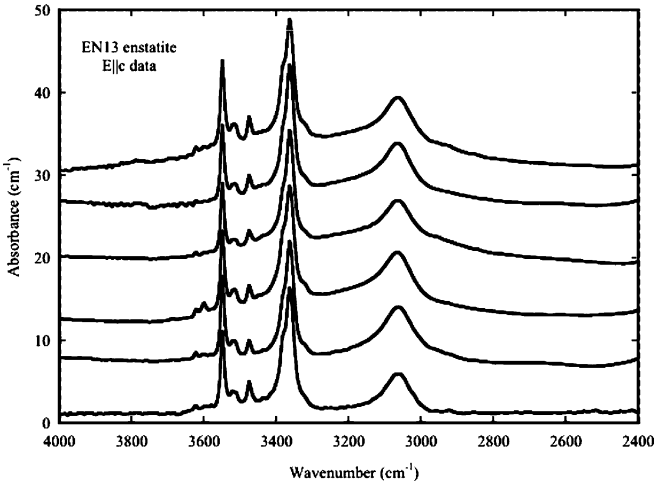


**Fig. 2** Series of spectra of EN13 from different crystals with varying amounts of the anistrotropic broad band contributing to the overall intensity. Note that the intensities of the narrow bands are very similar in all the spectra

OH band which is based on measurements on a range of hydrous minerals and allows for the observation that the integrated molar absorption coefficient is a strong function of vibrational frequency (and hence strength of hydrogen bonding) of the OH groups. The results of applying a similar calibration (Paterson 1982) are also presented here to aid comparison of our data with that from previous studies however it should be noted that throughout this paper the water contents of our synthetic phases were determined using Libowitzky and Rossman (1997). We consider the method of Libowitzky and Rossman (1997) to be preferable as it based on polarized measurements of crystalline materials, rather than the unpolarized measurements of gases, solutions and hydrous glasses which form the basis of the Paterson (1982) calibration. We also include, for completeness, the results of applying the mineral specific calibrations for orthopyroxene (Bell et al. 1995) and olivine (Bell et al. 2003) however, we do not favor the use of these calibrations for our data as they take no account of the highly variable nature of the IR spectrum for NAMs and may only be reliable for samples whose IR spectra match closely those of the samples used to construct the calibration (Bell et al. 2003).

## Results

### Run products

Euhedral enstatite crystals were recovered from all the experiments reported in this study. Most runs also contained olivine (see Table 1). All runs except EN3 contained small spheres, rods and dendritic structures composed almost entirely of $SiO_2$. These are interpreted as the results of quenching an aqueous fluid. In addition EN11 and EN13 contained unidentified Al-rich phases mixed in with the $SiO_2$ gel. EN3 contained slab like intergrowths of enstatite with some other interstitial material in patches too small to analyze. These intergrowths are interpreted as the product formed by quenching a hydrous melt with a composition close to $MgSiO_3$. The quenched melt phase was hard to distinguish from primary enstatite crystals. It is therefore possible that some other samples also contain a small amount of melt, but if so, it cannot be enough to sequester all the water as all the samples, apart from EN3, are clearly saturated with an excess aqueous phase Table 2.

Polarized infrared absorbance spectra of OH-defects in both olivine and orthopyroxene generate numerous, well defined bands in the region 4,000–2,800 $cm^{-1}$. Absorbance spectra of both phases show the presence and relative intensities of certain OH absorptions to be run-dependant. In all cases, the vibrational energy of OH defect bands on polarized spectra obtained from different crystals from the same experiment are essentially identical suggesting that equilibrium of the OH defect population throughout the capsule was attained.

### Water in enstatite

Polarized infrared absorbance spectra of enstatite are presented on Fig. 3. Enstatite spectra show a number of strongly polarized, OH-related absorption bands.

**Table 2** Average compositions of forsterite and enstatite crystals. Na, Ti, Ca, Mn and Fe were below detection limit

| Sample | *n* | $SiO_2$ | 1σ | MgO | 1σ | $Al_2O_3$ | 1σ | Total | 1σ |
|---|---|---|---|---|---|---|---|---|---|
| Forsterite | | | | | | | | | |
| EN1 | 27 | 42.10 | (0.28) | 57.97 | (0.32) | 0.001 | (0.001) | 100.1 | (0.55) |
| EN2 | 40 | 42.03 | (0.31) | 57.91 | (0.32) | 0.000 | (0.001) | 99.96 | (0.51) |
| EN4 | 12 | 41.99 | (0.16) | 57.88 | (0.17) | 0.002 | (0.002) | 99.96 | (0.29) |
| EN5 | 35 | 42.90 | (0.72) | 56.95 | (0.74) | 0.000 | (0.004) | 99.90 | (0.41) |
| EN6 | 15 | 42.04 | (0.11) | 57.30 | (0.50) | 0.000 | (0.000) | 99.39 | (0.15) |
| EN7 | 16 | 41.61 | (0.12) | 57.59 | (0.47) | 0.001 | (0.001) | 99.23 | (0.24) |
| EN8 | 8 | 42.35 | (0.19) | 57.85 | (0.18) | 0.000 | (0.001) | 100.2 | (0.31) |
| EN12 | 18 | 42.14 | (0.21) | 58.01 | (0.18) | 0.000 | (0.000) | 100.2 | (0.46) |
| Enstatite | | | | | | | | | |
| EN1 | 24 | 59.24 | (0.21) | 40.41 | (0.20) | 0.015 | (0.011) | 99.69 | (0.37) |
| EN2 | 23 | 59.48 | (0.29) | 40.62 | (0.48) | 0.044 | (0.009) | 100.2 | (0.56) |
| EN3 | 17 | 59.32 | (0.21) | 40.58 | (0.14) | 0.000 | (0.001) | 99.92 | (0.32) |
| EN4 | 9 | 58.18 | (0.57) | 40.00 | (0.30) | 0.067 | (0.008) | 98.29 | (0.91) |
| EN5 | 6 | 59.89 | (0.31) | 40.38 | (0.93) | 0.003 | (0.002) | 100.3 | (0.21) |
| EN6 | 14 | 60.18 | (0.20) | 40.38 | (0.15) | 0.048 | (0.008) | 100.7 | (0.21) |
| EN7 | 42 | 59.46 | (0.19) | 40.31 | (0.29) | 0.000 | (0.000) | 99.81 | (0.36) |
| EN8 | 21 | 59.43 | (0.25) | 40.63 | (0.26) | 0.001 | (0.001) | 100.1 | (0.48) |
| EN9 | 14 | 58.98 | (0.29) | 40.44 | (0.16) | 0.075 | (0.017) | 99.53 | (0.41) |
| EN11 | 35 | 58.94 | (0.42) | 40.89 | (0.28) | 0.119 | (0.029) | 99.77 | (0.40) |
| EN12 | 24 | 59.71 | (0.23) | 40.75 | (0.15) | 0.000 | (0.001) | 100.5 | (0.33) |
| EN13 | 21 | 59.72 | (0.30) | 40.72 | (0.16) | 0.121 | (0.033) | 100.6 | (0.45) |

Values in parenthesis represent one standard deviation
*n* number of analyses

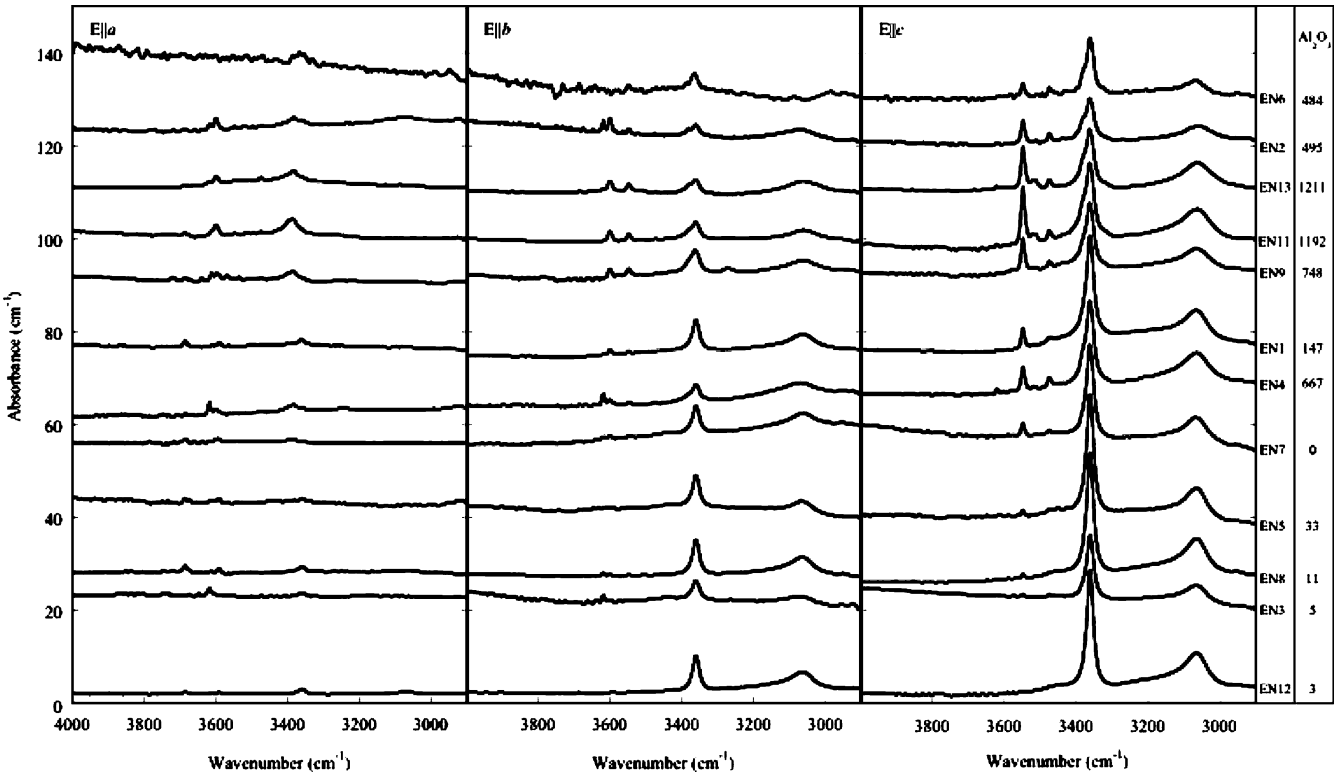


**Fig. 3** Polarized absorbance spectra of OH defect bands in oriented enstatite single crystals from each of the experiments

The vibrational energy and integrated absorbance of each OH-defect band are compiled on Table 3. OH absorptions in enstatite are strongest in measurements made with $E \parallel c$. $E \parallel c$ vibrations are dominated by a broad band at 3,062 $cm^{-1}$ and a sharper band at 3,363 $cm^{-1}$ but may be accompanied by additional bands at 3,380, 3,474, 3,515, and 3,547 $cm^{-1}$. Vibrations measured E || *b* are also dominated by two bands at 3,363 and 3,062 $cm^{-1}$, as observed in measurements made where $E \parallel c$, but may show additional absorptions at 3,381, 3,547, 3,600 and 3,617 $cm^{-1}$. Enstatite measured with E || *a* have relatively weak OH peaks. Measured where E || *a* enstatite crystals from runs EN1, EN6, EN7, EN8 and EN12 show an absorption centered at 3,363 $cm^{-1}$ accompanied by further bands at 3,687 and 3,590 $cm^{-1}$. E || *a* vibrations of enstatite from EN6 show a band at 3,382 $cm^{-1}$ accompanied by bands at 3,602 and 3,621 $cm^{-1}$. Enstatite from EN2, EN4, EN9, EN11 and EN13 show bands at 3,621, 3,602, 3,475 and 3,382 $cm^{-1}$. In each of the samples studied here OH defects in enstatite lie predominantly parallel to the *c*-axis of the crystal. The total amount of water dissolved in enstatite calculated from the total integrated absorbance derived following the baseline and background subtraction methods described in the previous section and by using the empirical IR calibration of Libowitzky and Rossman (1997) varies between 55 and 136 ppm $H_2O$ (Table 5).

In order to facilitate comparison with other published studies water solubility in enstatite calculated using the alternative calibrations of Paterson (1982) and Bell et al. (1995) are also given in Table 5. However, it should be noted that the changes in spectrum with addition of small quantities of Al (e.g., EN12 vs. EN13) mean that any IR calibration based on a fixed extinction coefficient (Bell et al. 1995) is unlikely to give the correct water concentrations for both samples. Using the Libowitzky and Rossman (1997) calibration suggests that addition of 1,200 ppm $Al_2O_3$ increases the solubility of water in enstatite at 2.0 GPa and 1,350°C from 119 to 133 ppm. This increased solubility is consistent with previous studies (Rauch and Keppler 2002; Stalder and Skogby 2002). Using the mineral specific calibration (Bell et al. 1995) would result in a slight decrease in solubility (Table 5), which is almost certainly incorrect.

## Water in forsterite

When measured with E || *a* the vibrations of OH defects in the studied olivines are dominated by absorptions in the frequency range 3,620–3,500 $cm^{-1}$ (Fig. 4; Table 4). The main bands are located at 3,623, 3,613, 3,590, and 3,578 $cm^{-1}$ but forsterite from EN1, EN4, EN5 and EN7 show a further well defined peak at 3,350 $cm^{-1}$. The E || *b* spectra of forsterite from EN6 and EN12 show no OH absorptions. E || *b* spectra of forsterite from EN2 show two strong bands at 3,600 and 3,350 $cm^{-1}$. E || *b* vibrations in forsterite from EN5 and EN8 are characterized by bands at 3,579 and

**Table 3** Results of quantifying FTIR spectra of enstatite. Columns 2–14 are the integrated absorbencies under each of the absorption bands along each orthogonal direction; columns 15–17 are the corresponding total water contents calculated for each direction individually and using three alternative calibrations

| | 3687 | 3649 | 3621 | 3602 | 3590 | 3549 | 3517 | 3475 | 3444 | 3380 | 3360 | 3121 | 3062 | $H_2O^a$ | $H_2O^b$ | $H_2O^c$ |
|---|---|---|---|---|---|---|---|---|---|---|---|---|---|---|---|---|
| E \|\| a | | | | | | | | | | | | | | | | |
| EN1 | 30.07 | 0 | 7.1 | 0 | 21.9 | 6.5 | 0 | 0 | 0 | 0 | 52.4 | 0 | 0 | 18.3 | 11.8 | 7.9 |
| EN2 | 0 | 0 | 19.7 | 42.4 | 0 | 0 | 0 | 4.9 | 0 | 66.8 | 22.1 | 0 | 0 | 15.4 | 11.1 | 10.5 |
| EN3 | 0 | 5.6 | 41.1 | 0 | 20.1 | 0 | 0 | 0 | 0 | 6.7 | 25.5 | 0 | 0 | 10.8 | 7.6 | 5.8 |
| EN4 | 0 | 0 | 49.2 | 22 | 0 | 0 | 0 | 3.7 | 0 | 56.7 | 19.2 | 0 | 0 | 16.7 | 11.8 | 10.1 |
| EN5 | 16.4 | 8.5 | 13.3 | 0 | 21.2 | 0 | 0 | 0 | 0 | 17.1 | 29.1 | 0 | 0 | 15.9 | 10.5 | 7.1 |
| EN6 | 0 | 0 | 0 | 0 | 0 | 0 | 0 | 0 | 0 | 0 | 76.4 | 0 | 0 | 4.6 | 3.4 | 5.1 |
| EN7 | 21.4 | 0 | 10.1 | 22.3 | 0 | 22.6 | 0 | 0 | 0 | 23.8 | 16.9 | 0 | 0 | 17.1 | 11.4 | 7.9 |
| EN8 | 25.5 | 6.7 | 8.4 | 0 | 167.0 | 0 | 0 | 0 | 0 | 0 | 42.3 | 0 | 0 | 16.8 | 10.7 | 6.9 |
| EN9 | 20.3 | 0 | 18.1 | 21.8 | 0 | 0 | 0 | 4.7 | 0 | 83.2 | 14.2 | 0 | 0 | 19.1 | 12.9 | 10.4 |
| EN11 | 23.1 | 0 | 21.2 | 38.2 | 0 | 0 | 0 | 5.2 | 0 | 89.2 | 14.8 | 0 | 0 | 23.9 | 16.2 | 12.9 |
| EN12 | 25.7 | 3.5 | 12.1 | 0 | 16.6 | 0 | 0 | 0 | 0 | 0 | 75.3 | 0 | 0 | 18.9 | 12.4 | 9.0 |
| EN13 | 13.3 | 0 | 10.1 | 26.1 | 0 | 10.0 | 0 | 9.4 | 0 | 83.3 | 19.3 | 0 | 0 | 17.9 | 12.5 | 11.3 |
| E \|\| b | | | | | | | | | | | | | | | | |
| EN1 | 0 | 0 | 0 | 10.0 | 0 | 7.7 | 0 | 0 | 0 | 0 | 194.0 | 92.0 | 199.0 | 23.5 | 18.1 | 33.9 |
| EN2 | 0 | 0 | 25.0 | 44.0 | 0 | 17.0 | 0 | 4.7 | 0 | 38 | 86.0 | 0 | 408.0 | 33.7 | 25.3 | 41.9 |
| EN3 | 0 | 0 | 20.0 | 6.6 | 0 | 0 | 0 | 0 | 0 | 0 | 154.0 | 0 | 283.0 | 22.5 | 17.2 | 31.2 |
| EN4 | 0 | 0 | 31.1 | 11.1 | 0 | 9.2 | 0 | 0 | 0 | 15.2 | 116.2 | 0 | 326.7 | 26.1 | 19.6 | 33.7 |
| EN5 | 0 | 0 | 0 | 0 | 0 | 0 | 0 | 0 | 0 | 0 | 274 | 0 | 251.0 | 24.1 | 18.7 | 35.3 |
| EN6 | 0 | 0 | 0 | 0 | 0 | 15.0 | 0 | 0 | 0 | 17 | 106 | 0 | 0 | 8.7 | 6.7 | 9.2 |
| EN7 | 0 | 0 | 9.6 | 12 | 0 | 6.1 | 0 | 0 | 22 | 0 | 187 | 0 | 425.6 | 28.9 | 22.3 | 43.3 |
| EN8 | 0 | 0 | 8.6 | 5 | 0 | 3.7 | 0 | 0 | 0 | 0 | 240 | 115 | 277.0 | 29.7 | 22.9 | 43.7 |
| EN9 | 0 | 0 | 0 | 42.5 | 0 | 29.8 | 0 | 1.8 | 0 | 65.9 | 115.8 | 62.5 | 234.6 | 30.5 | 23.0 | 37.3 |
| EN11 | 0 | 0 | 0 | 37.0 | 0 | 31.0 | 0 | 2.5 | 0 | 85 | 89 | 0 | 356.0 | 31.0 | 23.6 | 40.5 |
| EN12 | 0 | 0 | 0 | 0 | 0 | 1.8 | 0 | 0 | 0 | 0 | 243.0 | 135.0 | 272.0 | 27.9 | 22 | 43.9 |
| EN13 | 0 | 0 | 0 | 77.0 | 0 | 49 | 27 | 4.2 | 0 | 72 | 75.0 | 0 | 522.0 | 45.9 | 34.5 | 55.9 |
| E \|\| c | | | | | | | | | | | | | | | | |
| EN1 | 0 | 0 | 0 | 0 | 0 | 56.3 | 0 | 15.4 | 11.5 | 0 | 693.0 | 174.0 | 497.0 | 71.1 | 54.8 | 97.5 |
| EN2 | 0 | 0 | 0 | 0 | 0 | 81.0 | 0 | 27.9 | 0 | 33.0 | 267.0 | 71.5 | 278.0 | 40.3 | 30.8 | 51.1 |
| EN3 | 0 | 0 | 0 | 0 | 0 | 2.3 | 0 | 10.3 | 0 | 102.0 | 371.0 | 37.0 | 213.0 | 39.0 | 30.1 | 53.3 |
| EN4 | 0 | 0 | 2.4 | 0 | 0 | 67.2 | 5.9 | 23.7 | 0 | 106.7 | 582.3 | 35.6 | 458.2 | 68.1 | 51.9 | 84.1 |
| EN5 | 0 | 0 | 0 | 0 | 0 | 5.9 | 0 | 0 | 69.3 | 84.0 | 669.0 | 111.0 | 367.0 | 65.5 | 50.6 | 88.0 |
| EN6 | 0 | 0 | 0 | 0 | 0 | 37.5 | 0 | 30.2 | 0 | 86.7 | 344.0 | 82.9 | 182.0 | 41.7 | 32.1 | 52.1 |
| EN7 | 0 | 0 | 0 | 0 | 0 | 41.1 | 0 | 6.5 | 0 | 75.2 | 356.7 | 62.0 | 386.4 | 45.1 | 34.8 | 62.5 |
| EN8 | 0 | 0 | 0 | 0 | 0 | 4.8 | 0 | 22.1 | 0 | 141.0 | 818.0 | 198.0 | 450.0 | 72.4 | 56.2 | 101.8 |
| EN9 | 0 | 0 | 1.7 | 0 | 0 | 132.6 | 6.9 | 19.8 | 0 | 171.0 | 328.5 | 0 | 668.9 | 68.6 | 52.5 | 89.6 |
| EN11 | 0 | 0 | 2.9 | 0 | 0 | 160.0 | 20.1 | 25.3 | 0 | 290.0 | 334.0 | 0 | 686.0 | 81.3 | 62.1 | 102.3 |
| EN12 | 0 | 0 | 0 | 0 | 0 | 0.9 | 0 | 0 | 19.4 | 0 | 841.0 | 215.0 | 452.0 | 72.6 | 56.3 | 102.9 |
| EN13 | 0 | 0 | 2.3 | 0 | 0 | 148.0 | 24.4 | 31.8 | 0 | 296.0 | 242.0 | 0 | 467.0 | 68.7 | 52.3 | 81.6 |

$H_2O$ concentrations estimated using [a]Libowitzky and Rossman, [b]Paterson, [c]Bell et al. calibrations

3,555 $cm^{-1}$. OH bands measured with E || *c* for samples EN1 EN5, EN7 and EN12 show a broad absorption centered at 3,160 $cm^{-1}$ whilst EN6 shows a broad band at 3,217 $cm^{-1}$ and forsterite from sample EN2 shows absorptions at both 3,217 and 3,160 $cm^{-1}$. Spectra measured with E || *c* in samples EN1, EN2, EN4 and EN7 show strong bands at 3,347 and 3,323 $cm^{-1}$. Along this crystallographic direction a further band 3,405 $cm^{-1}$ is also observed in forsterite from sample EN1. OH defects in near end member forsterite are mostly aligned parallel to the *a* and *c* axes. Distribution of OH between the two orientations is approximately 1:1. Water solubility in forsterite is essentially constant for the samples synthesized here (Table 5). When the total integrated OH absorbance is converted to water contents using the calibration of Libowitzky and Rossman (1997) forsterite crystals synthesized in this study contain between 36 and 44 ppm $H_2O$. As with enstatite, water solubilities calculated using the calibrations of Paterson (1982) and Bell et al. (2003) are also given in Table 5 for comparative purposes.

## Discussion

### OH-defects and dissolved $H_2O$ concentrations on enstatite

The data presented above can be used to explain a number of different aspects of OH dissolution in orthopyroxene. The amount of water dissolved in enstatite crystals synthesized under different conditions varies significantly (Table 5). Enstatite water contents are considerably lower in the "low temperature" run EN6, which was carried out at 2.0 GPa and 1,100°C; enstatite in EN6 contains 59 ppm $H_2O$, compared with an average of 114 ppm $H_2O$ for the other samples synthesized at 2.0 GPa and 1,350°C. The effect of pressure is less

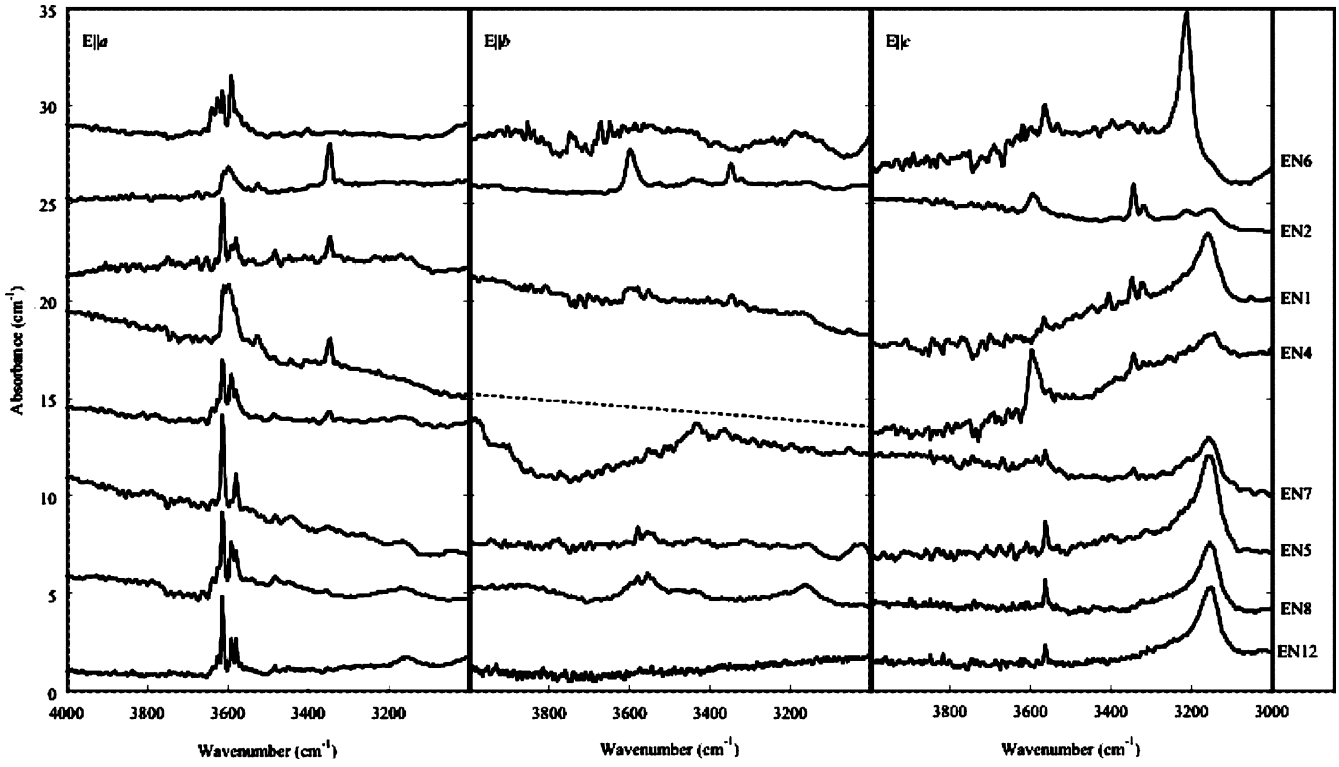


**Fig. 4** Polarized absorbance spectra of OH defect bands in oriented forsterite single crystals from each of the experiments

**Table 4** Results of quantifying FTIR spectra of forsterite. Columns 2–18 are the integrated absorbencies under each of the absorption bands along each orthogonal direction; columns 19–20 are the corresponding total water contents calculated for each direction individually and using two alternative calibrations

| | 3637 | 3623 | 3614 | 3600 | 3590 | 3579 | 3568 | 3555 | 3525 | 3484 | 3442 | 3403 | 3382 | 3345 | 3320 | 3216 | 3165 | $H_2O^a$ | $H_2O^b$ |
|---|---|---|---|---|---|---|---|---|---|---|---|---|---|---|---|---|---|---|---|
| E \|\| *a* | | | | | | | | | | | | | | | | | | | |
| EN1 | 0 | 0 | 46 | 0 | 15.0 | 25.6 | 0 | 0 | 0 | 11.6 | 0 | 0 | 0 | 25.6 | 8.1 | 0 | 0 | 15.6 | 11.1 |
| EN2 | 0 | 0 | 9.0 | 32.0 | 9.8 | 11.6 | 0 | 0 | 10.1 | 0 | 2.4 | 0 | 6.8 | 39.8 | 5.1 | 0 | 0 | 13.1 | 9.4 |
| EN4 | 0 | 0 | 34.7 | 53.2 | 39.2 | 24.9 | 0 | 16.9 | 26.7 | 3.0 | 1.8 | 4.5 | 3.9 | 33.2 | 0 | 0 | 0 | 29.4 | 20.9 |
| EN5 | 6 | 0 | 70.3 | 0 | 0 | 31.8 | 0 | 0 | 0 | 6.4 | 0 | 0 | 0 | 10.0 | 0 | 0 | 0 | 17.9 | 12.5 |
| EN6 | 14.6 | 20.3 | 29.7 | 0 | 36.0 | 8.5 | 13.1 | 9.7 | 0 | 0 | 0 | 10.7 | 0 | 0 | 0 | 0 | 0 | 20.7 | 14.5 |
| EN7 | 7.0 | 9.9 | 49.2 | 0 | 37.0 | 14.6 | 0 | 0 | 0 | 10.2 | 0 | 0 | 0 | 12.8 | 0 | 0 | 0 | 19.7 | 13.8 |
| EN8 | 12.5 | 21.5 | 70.2 | 0 | 21.4 | 19.8 | 0 | 0 | 0 | 6.2 | 0 | 0 | 0 | 0 | 0 | 0 | 0 | 23.7 | 16.4 |
| EN12 | 4.6 | 10.2 | 64.7 | 0 | 11.6 | 16.4 | 6.2 | 0 | 0 | 4.2 | 0 | 0 | 0 | 0 | 0 | 0 | 0 | 18 | 12.6 |
| E \|\| *b* | | | | | | | | | | | | | | | | | | | |
| EN1 | 0 | 0 | 0 | 12.4 | 0 | 13.7 | 0 | 10.0 | 0 | 0 | 0 | 0 | 1.3 | 12.9 | 6.7 | 0 | 0 | 6.0 | 4.3 |
| EN2 | 0 | 0 | 0 | 46.2 | 0 | 21.2 | 0 | 0 | 3.7 | 0 | 6.0 | 5.1 | 1.1 | 22.6 | 6.8 | 0 | 0 | 12.6 | 9 |
| EN4 | nd | nd | nd | nd | nd | nd | nd | nd | nd | nd | nd | nd | nd | nd | nd | nd | nd | nd | nd |
| EN5 | 0 | 0 | 0 | 0 | 0 | 9.6 | 0 | 8.2 | 7.6 | 0 | 0 | 0 | 1.2 | 0 | 0 | 0 | 0 | 3.1 | 2.2 |
| EN6 | 0 | 0 | 0 | 0 | 0 | 0 | 0 | 0 | 0 | 0 | 0 | 0 | 0 | 0 | 0 | 0 | 0 | 0 | 0 |
| EN7 | 0 | 0 | 0 | 0 | 0 | 0 | 0 | 0 | 0 | 0 | 0 | 0 | 0 | 0 | 0 | 0 | 0 | 0 | 0 |
| EN8 | 0 | 0 | 0 | 0 | 0 | 6.2 | 0 | 5.9 | 0 | 0 | 0 | 0 | 0 | 0 | 0 | 0 | 0 | 1.5 | 1.1 |
| EN12 | 0 | 0 | 0 | 0 | 0 | 0 | 0 | 0 | 0 | 0 | 0 | 0 | 0 | 0 | 0 | 0 | 0 | 0 | 0 |
| E \|\| *c* | | | | | | | | | | | | | | | | | | | |
| EN1 | 0 | 0 | 0 | 0 | 0 | 14.9 | 0 | 0 | 0 | 0 | 0 | 9.8 | 0 | 24.9 | 14.1 | 70.5 | 278.5 | 18 | 14.1 |
| EN2 | 0 | 0 | 0 | 14.9 | 9.2 | 0 | 8.3 | 0 | 0 | 0 | 0 | 0 | 0 | 33.8 | 13.2 | 26.4 | 64.5 | 10.6 | 8.0 |
| EN4 | 0 | 0 | 0 | 29.3 | 14.2 | 0 | 0 | 14.5 | 0 | 0 | 0 | 0 | 0 | 13.4 | 0 | 0 | 79.8 | 10.3 | 7.6 |
| EN5 | 0 | 0 | 0 | 0 | 0 | 0 | 25.5 | 0 | 0 | 0 | 0 | 0 | 0 | 0 | 0 | 140.4 | 250.6 | 18.6 | 14.4 |
| EN6 | 0 | 0 | 0 | 0 | 0 | 0 | 33.1 | 0 | 0 | 0 | 0 | 0 | 0 | 0 | 0 | 374.7 | 7.5 | 20.2 | 15.6 |
| EN7 | 0 | 0 | 0 | 0 | 12.2 | 0 | 22.0 | 0 | 0 | 0 | 0 | 0 | 0 | 8.3 | | 127.6 | 262.3 | 20.2 | 15.5 |
| EN8 | 0 | 0 | 0 | 0 | 0 | 0 | 26.1 | 0 | 0 | 0 | 0 | 0 | 0 | 0 | 0 | 142.6 | 250.9 | 18.9 | 14.6 |
| EN12 | 0 | 0 | 0 | 0 | 0 | 0 | 18.4 | 0 | 0 | 0 | 0 | 0 | 0 | 0 | 0 | 146.9 | 242.2 | 17.6 | 13.7 |

$H_2O$ contents estimated using [a]Libowitzky and Rossman; [b]Paterson 1982

**Table 5** Water concentrations of forsterite and enstatite calculated using the ($H_2O^{Lib}$) Libowitzky and Rossman (1997), ($H_2O^{Pat}$) Paterson (1982), and ($H_2O^{Bell}$) Bell (1995, 2004) calibrations, and the water partition coefficient, $D_{H_2O}^{en/ol}$, calculated using the $H_2O^{Lib}$ data

| | Forsterite | | | Enstatite | | | $D_{H_2O}^{en/ol}$ |
|---|---|---|---|---|---|---|---|
| | $H_2O^{Lib}$ | $H_2O^{Pat}$ | $H_2O^{Bell}$ | $H_2O^{Lib}$ | $H_2O^{Pat}$ | $H_2O^{Bell}$ | |
| EN1 | 40 | 30 | 118 | 113 | 85 | 139 | 2.83 |
| EN2 | 36 | 26 | 80 | 89 | 67 | 103 | 2.47 |
| EN3 | – | – | – | 72 | 55 | 90 | – |
| EN4[a] | > 40 | > 29 | > 77 | 111 | 83 | 128 | < 2.77 |
| EN5 | 40 | 29 | 111 | 106 | 80 | 130 | 2.72 |
| EN6 | 41 | 30 | 109 | 55 | 45 | 66 | 1.34 |
| EN7 | 40 | 29 | 112 | 91 | 69 | 114 | 2.28 |
| EN8 | 44 | 32 | 114 | 119 | 90 | 152 | 2.70 |
| EN9 | – | – | – | 118 | 88 | 137 | – |
| EN11 | – | – | – | 136 | 102 | 156 | – |
| EN12 | 36 | 26 | 103 | 119 | 91 | 156 | 3.31 |
| EN13 | – | – | – | 133 | 99 | 149 | – |

[a]For EN4, only the E|| *a* and E|| *c* orientations are available for olivine

pronounced; enstatite in EN2, synthesized at 1.0 GPa and 1,350°C contains 89 ppm compared with 114 ppm average for 2.0 GPa and 1,350°C.

There is excellent correlation between the amount of aluminum in enstatite and the nature of the OH absorbance spectrum. The spectrum of the purest enstatite sample, EN12, is dominated by two distinct OH bands at 3,360 and 3,060 $cm^{-1}$. The integrated absorbance of the absorptions centered at 3,549 and 3,380 $cm^{-1}$ on spectra measured with E || *b* and E || *c* increase systematically with the Al content of the crystal (Fig. 5). Spectra measured where E || *b* also show a correlation between the band centered at 3,602 $cm^{-1}$ and Al content. The correlation between enstatite $Al_2O_3$ content and additional peaks on OH stretching spectra is illustrated more clearly in Fig. 5. In Fig. 5 the y-axis represents water concentrations calculated individually for three minor peaks (by summing the intensities from all three directions and applying the calibration of Libowitzky and Rossman 1997), then normalizing by the water concentration corresponding to the 3,360 $cm^{-1}$ peak. Normalizing allows all the samples from different temperatures, pressures and water concentrations to be compared. Figure 5 shows that the water concentrations corresponding to the 3,380, 3,475 and 3,549 $cm^{-1}$ peaks all show a good or excellent linear correlation with the $Al_2O_3$ concentration considering the substantial errors in Al analysis at these low concentrations.

Apart from in EN11 and EN13 the aluminum in the samples is an accidental contaminant. The source of this contamination is not known but could be from a mortar and pestle, $Al_2O_3$ dust in the vicinity of starting mixture preparation, or even diffusion from the crushable alumina sleeve through the Pt capsule during the high pressure and temperature experiment. However, examination of spectra in the literature for enstatite samples reported to be pure $MgSiO_3$ suggests that other workers may have had similar problems. Many of the pure enstatite spectra reported by Mierdel and Keppler (2004) and to a lesser extent Rauch and Keppler (2002) also contain peaks at 3,320, 3,380, 3,475 and 3,550 $cm^{-1}$. Our data strongly suggest that these peaks are related to aluminum contamination and in the case of Mierdel and Keppler (2004) the amount of aluminum appears to be larger than most of our samples. Precisely comparing the relative heights of these aluminum-related OH bands between samples synthesized in different studies is difficult, but if minor differences in pressure and temperature can be ignored, the relative intensities of aluminum-related OH bands correlate with aluminum contents in a manner similar to that proposed as suggested here proves correct up to (1,000 ppm $Al_2O_3$ may contaminate enstatite crystals reported by Mierdel and Keppler (2004). Aluminum incorporation is known to increase the solubility of $H_2O$ in enstatite (Rauch and Keppler 2002; Stalder 2004), so the solubility data of Mierdel and Keppler (2004) could require a minor correction. However, at the level of Al incorporated in the present study the enhancement in OH solubility is small.

As previous studies have suggested that crystal growth rate can have a significant effect on the on the concentration of OH defects incorporated into synthetic forsterite (Lemaire et al. 2004) controlled experiments were performed to test this possibility for enstatite. Comparison of EN9 (cooled at 1,000°C/h from 1,420°C to 1,350°C) and EN12 (cooled at 2°C/h over the same temperature interval) showed no significant difference in water concentrations. Similarly the two samples with deliberately added $Al_2O_3$, EN11 and EN13, both had different cooling histories (see Table 1) but no significant difference in water concentration or OH defect population was observed.

Experiment EN3 contained only enstatite and melt; there is no evidence for a free aqueous phase. EN3 was therefore not used to evaluate the effect of temperature on water solubility in enstatite, however, the amount of water in the melt in this sample can be very crudely estimated and an approximate value for $D_{H_2O}^{en/melt}$ calculated. The melt must contain more than 9 wt% water (the bulk water concentration of the capsule) and less than 20 wt% water (the estimated maximum water solubility (Inoue 1994)). As the sample contains abundant

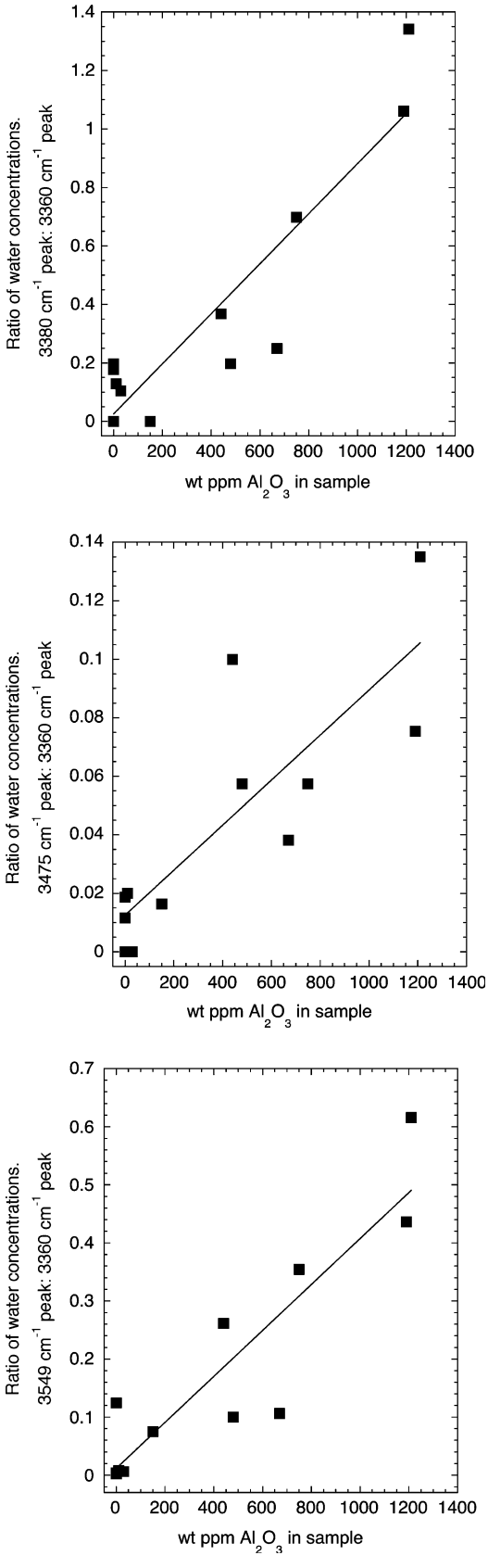


**Fig. 5** The effect of aluminum incorporation on the mechanism of water incorporation in enstatite. The parameter plotted on the y-axis was obtained by summing the water concentrations (calculated using the Libowitzky and Rossman (1997) calibration, Table 3) in each of the 3 directions, then taking the ratio of the 3,380, 3,475 and 3,549 $cm^{-1}$ water concentrations to the that of the large peak at 3,360 $cm^{-1}$. Scaling the water concentrations by that of the 3,360 $cm^{-1}$ band enables samples made at different pressures, temperatures and water concentrations to be compared. The straight lines are linear fits to the data

enstatite crystals, which would enrich the melt in water, it is probable that the water concentration in the melt was closer to 20 than 10%, so we make the assumption of a melt water concentration of 18 wt%, giving $D_{H_2O}^{en/melt} = 3.9 \times 10^{-4}$. This is very low compared to previous estimates of 1.3–2.7×$10^{-2}$ (Aubaud et al. 2004), 2.45×$10^{-2}$ (Koga et al. 2003), 2−5×$10^{-3}$ (Grant et al. 2004; Grant et al. in preparation), 3–4×$10^{-3}$ (Dobson et al. 1995). The reasons for the difference cannot be fully appreciated until more experimental data are published but are at least partly related to the very low aluminum concentration in EN3, different analytical methods and differing IR calibrations.

Our data can be compared directly with previous data which describe water solubility in enstatite published by Kohn (1996), Rauch and Keppler (2002), Stalder (2002, 2004), Mierdel and Keppler (2004), and Najorka and Kohn (in preparation) in the pure $MgO–SiO_2–H_2O$ and $MgO–SiO_2–Al_2O_3–H_2O$ systems. Figure 6 summarizes the solubility of water in pure enstatite reported in different IR studies, as calculated using the Paterson (1982) calibration. Rauch and Keppler (2002) studied the effect of pressure on the solubility of water in pure enstatite at 1,100°C, and found the solubility to be around 130 ppm at 1.5 and 2.5 GPa [using the calibration of Paterson (1982)], compared with the value of 45 ppm for 1,100 C and 2.0 GPa (using the same calibration) in this study. This discrepancy can probably be attributed entirely to the methods used to process the spectra; our solubilities are in much better agreement with the data of Mierdel and Keppler (2004), using the data processing method where they only include intensity from the sharp bands (effectively equivalent to the methods employed in the present study). Water solubilities reported by Stalder (2002, 2004) are much higher than other studies being around 200 ppm $H_2O$ [recalculated using the Paterson (1982) calibration] in pure enstatite synthesized at 2.5 GPa and 1,150°C. The high values appear to be due to the use of a linear baseline, which we consider to be unrealistic for our samples. In summary, the differences between the reported solubilities from IR studies of experimentally produced enstatite can be reconciled if the different calibrations and baseline and background corrections are taken in to account. Having said that, NMR data (Kohn 1996) and a more detailed recent

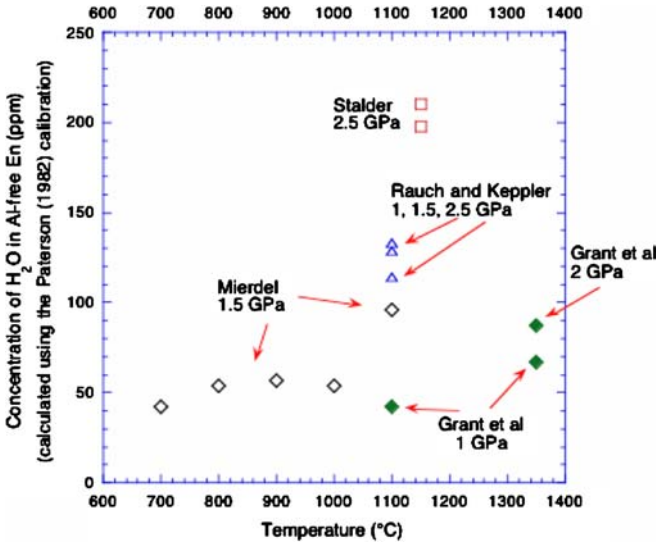


**Fig. 6** Comparison of the $H_2O$ concentration in Al-free enstatite from different studies. In all cases, the concentrations are calculated or recalculated using the Paterson (1982) calibration. The data are taken from this study (*filled diamonds*); Mierdel and Keppler (2004) (*open diamonds*); *triangles* (Rauch and Keppler (2002)) and Stalder and Skogby (2002) (*squares*)

NMR study (Najorka and Kohn, in preparation), give solubilities of around 200–240 ppm under similar pressure and temperature conditions, suggesting that the Bell et al. (2004) calibration may give better absolute results even though theoretically a wavenumber-dependent calibration is more likely to be transferable between different samples.

As noted previously Rauch and Keppler (2002) and Stalder (2004) also studied the effect of aluminum on the amount of water dissolved in enstatite. Both studies concluded that water solubility increased as a function of $Al_2O_3$ concentration. The increased in water solubility observed in the present study is smaller than that predicted by Rauch and Keppler (2002), but in better agreement with Stalder and Skogby (2002) and Stalder (2004). These differences can perhaps be ascribed to differences in the silica activity.

## OH-defects and dissolved $H_2O$ concentrations on forsterite

There is controversy over the interpretation of the OH stretching spectra of olivine. Although OH absorptions in the 3,500–3,650 $cm^{-1}$ region have been attributed to OH associated with Mg or Fe vacancies in the olivine structure (Bai and Kohlstedt 1993; Kohlstedt et al. 1996), there is increasing evidence to suggest that these bands may be due to OH groups which stabilize Si vacancies in olivine (Braithwaite et al. 2003; Brodholt 1997; Berry et al. 2005). It has also been suggested that low frequency bands at either at 3,300–3,400 $cm^{-1}$ (Matveev et al. 2001; Matveev et al. 2005) or 3,150–3,250 $cm^{-1}$ (Lemaire et al. 2004) represent hydrogen charge balancing octahedral site vacancies. The situation is complicated by the fact that the defect hydrogen concentration in olivine is around the same as other trace elements and it has recently been argued that Ti is crucial in determining both the incorporation mechanism and solubility of H in olivine (Berry et al. 2005).

The OH stretching spectra for forsterite (Fig. 4) are broadly similar to those reported by Lemaire et al. (2004) for forsterite grown under conditions of relatively high silica activity. They show broad peaks at 3,160 and 3,230 $cm^{-1}$ in addition to higher frequency bands. They are therefore consistent with the overall picture of OH defects in forsterite as a function silica activity described by Lemaire et al. (2004) in that the broad, low frequency peaks attributed to H substitution in Mg vacancies are large and the narrow high frequency peaks attributed to H substitution in Si vacancies are relatively small in the high silica system studied here. In detail the new data do suggest that some fine-tuning of the model of Lemaire et al. (2004) may be necessary. Firstly no correlation between the peaks at 3,230 and 3,600 $cm^{-1}$ is observed here and so these peaks do not appear to be diagnostic of the highest silica activities. Indeed, as all the forsterite crystals studied here coexist with enstatite it appears that 3,160 $cm^{-1}$ alone is the signature for Mg vacancies. The OH stretching spectrum of forsterite from EN12 in particular appears to be a simple and clean "ideal" spectrum for pure forsterite in equilibrium with enstatite. It is possible that the large peak at 3,216 $cm^{-1}$ [equivalent to 3,230 $cm^{-1}$ in Lemaire et al. (2004)] in EN6 is related to the lower temperature of this run compared with all the others. Alternatively, a different Mg vacancy may become more energetically favorable at lower temperatures. It is interesting to note that the two natural samples from Zabargad presented in Lemaire et al. (2004) both have the 3,230 $cm^{-1}$ peak rather than 3,160 $cm^{-1}$ and both are probably equilibrated at lower temperatures (especially the hydrothermal olivine with the 3,230 $cm^{-1}$ peak dominating the whole spectrum). Interpreting the small peaks in the range 3,300–3,500 $cm^{-1}$ proves more problematic. These peaks are clearly visible in random spectra from Lemaire et al. (2004) and this study and are best seen with E || *a* (Fig. 4). These are also the peaks considered by Matveev et al. (2001) to represent OH-defects in metal vacancies of natural mantle olivine compositions equilibrated at higher silica activity (enstatite bufferered). Matveev et al. (2005) have also shown these features replacing the high frequency peaks (3,500–3,650 $cm^{-1}$) in natural olivine phenocrysts as a function of increasing silica activity in the host melt. As these peaks are more prominent in complex natural compositions, it is tempting to associate them with metal impurities in our samples, although it is beyond the scope of this study to confirm this. It may be that the peaks are characteristic of Mg vacancies associated with some metal cation that is a major component of natural systems but only found in accidental and random trace amount in this study and Lemaire et al. (2004) or some more complex metal interaction.

For example shifts in peak positions are observed in the higher frequency peaks when Ti is added to the system (Berry et al. 2005). Again the Zabargad samples in Lemaire et al. (2004) are interesting as although they are natural compositions they show the characteristics of our pure end-members forsterites with 3,230 $cm^{-1}$ rather than 3,300–3,500 $cm^{-1}$ peaks.

The solubility of water in forsterite found here is lower than all but one of the samples described by Lemaire et al., (2004) which were synthesized under similar conditions and analyzed using essentially identical methods. The main difference between the two studies is that Lemaire et al. (2004) used higher Mg/Si ratios thus, with one exception, their samples did not coexist with enstatite. At 2.0 GPa, Lemaire et al. (2004) calculated approximately 60–70 ppm $H_2O$ in forsterite synthesized by cooled from higher temperatures and then held at 1,250–1,275°C compared with 100–110 ppm $H_2O$ in samples directly cooled to 1,400–1,430°C. The exceptions are sample Fo#1 which had an extremely high but non-equilibrium (unreproducible) water concentration and Fo#5 which had a low water concentration of 42 ppm in the forsterite, but also contained coexisting enstatite at 1,250°C. The water concentrations of forsterite crystals in the present study are all in the range 36–44 ppm at 2.0 GPa and all coexist with enstatite. Thus it appears that in the MSH system water solubility in forsterite is lower if enstatite is also present, and presumably buffering the system. This could be explained by considering the composition of the coexisting fluid phase. In enstatite-absent conditions the fluid can be water rich and silica poor, but in enstatite present conditions the composition of the fluid phase is $SiO_2$ buffered and is constrained to be higher than in the enstatite-absent case. The data summarized here illustrate that the concept of water solubility in a nominally anhydrous mantle mineral is questionable, because the water concentration in a NAM in equilibrium with an aqueous fluid will depend on the composition of the fluid, which is itself a function of temperature pressure, pressure and the bulk composition of the system. Experimental programs must therefore be very carefully planned if they are to provide useful and relevant data. Note that Matveev et al. (2001) also proposed that the solubility of water is much higher (by an order of magnitude) in the presence of magnesiowustite (low silica activity) than in the presence of orthopyroxene (high silica activity), but in their case the nature of the spectrum was completely different. Despite the differences in sample chemistry and nature of the olivine spectra, the water concentrations reported by Matveev et al. (2001) for orthopyroxene buffered olivine are comparable with the values found in the present study.

## Water partitioning between enstatite and forsterite

Very few data on partitioning of water between different NAMs exist. Values for $D_{H_2O}^{opx/ol}$ that have been published vary significantly and the effects of pressure, temperature and composition on hydrogen partitioning remain completely unexplored. Hirth and Kohlstedt (1996) combined previously published experimental data on the solubility in olivine, with analyses of the water concentrations in a natural orthopyroxene/melt pair to predict a value of $D_{H_2O}^{opx/ol} = 5$ under mantle conditions [based on the IR calibration of Paterson (1982)]. Hydrogen dissolved in natural phases entrained as xenocrysts in a kimberlite yield $D_{H_2O}^{opx/ol}$ of $1.6 \pm 0.2$ ($1\sigma$, $n = 11$) (Bell et al. 2004). $D_{H_2O}^{opx/ol}$ values calculated following synchrotron FTIR measurements made on mantle xenoliths vary between 3 and 69 (Grant et al. in preparation). $D_{H_2O}^{opx/ol} = 12 \pm 4$ ($2\sigma$, $n = 1$) was calculated from ion probe analyses of orthopyroxene and olivine synthesized at high pressure and temperature (Koga et al. 2003) and Aubaud et al. (2004) used ion probe data (ultimately calibrated using the bulk analyses used to calibrate IR by Bell et al. (1995, 2003)), on experimental samples equilibrated under similar conditions to those of this study, to report an average value of $D_{H_2O}^{opx/ol} = 9$. Most of the samples in the present study contained both forsterite and enstatite and can be used to obtain values for $D_{H_2O}^{opx/ol}$. Samples EN5, EN1 and EN8 were all synthesized at 2.0 GPa and 1,350°C, but had 18, 9 and 4.5 wt% water, respectively, in the capsules. They all have the same phase assemblage of enstatite, forsterite and fluid, so if they are all in equilibrium they should have the same phase compositions. EN1 is contaminated by a small amount of Al (147 ppm in the enstatite), but this small amount is not expected to significantly influence water solubilities or partitioning. The dissolved water concentrations in enstatite in the three samples are 106, 113 and 119 ppm, respectively; for forsterite the solubilities are 40, 40 and 44 ppm. Partition coefficients $D_{H_2O}^{en/fo}$ are therefore 2.72, 2.83 and 2.70, respectively. Excellent agreement between $D_{H_2O}^{en/fo}$ values calculated for each of these three samples suggests that equilibrium is attained in the experiments and demonstrates the reproducibility of the methods we have used to process the FTIR spectra. The data also provide information on the effect of temperature and pressure on $D_{H_2O}^{en/fo}$. EN6 was synthesized at 1,100°C and 2.0 GPa and has $D_{H_2O}^{en/fo} = 1.34$, much lower than the value of $D_{H_2O}^{en/fo} = 2.7$ for 1,350°C and 2.0 GPa. This difference arises from the strong temperature dependence of OH solubility in enstatite. The effect of pressure is less pronounced than the effect of temperature as $D_{H_2O}^{en/fo} = 2.47$ for 1,350°C and 1.0 GPa compared with $D_{H_2O}^{en/fo} = 2.7$ for 1,350°C and 2.0 GPa. Unfortunately, none of thealuminum-bearing experiments in this study yielded olivine crystals. The effect of incorporating additional elements into the starting mixture is currently the object of further investigation, however, preliminary results suggests that incorporating aluminum increases the solubility of water in orthopyroxene whilst that of olivine in significantly decreased (Grant et al. 2004),

giving a large increase in $D_{H_2O}^{en/fo}$. Many more experiments are obviously required to investigate the influence of major and trace element composition on the solubility and partitioning of water in NAMs, but it is clear that experiments must be very carefully planned if the effects of temperature, pressure and composition of crystalline, melt and fluid phases are to be disentangled.

## Conclusions

Following careful analysis of the OH absorbance spectra recorded on synthetic enstatite suggests that some of the intensity is likely related to non-point defect OH. Great care must therefore be taken in comparing water concentrations derived in different studies, especially if different background subtractions and different calibrations were applied.

The solubility of water in enstatite found in the present study is in the range 55–133 ppm [based on the Libowitzky and Rossman (1997) calibration] and shows strong temperature dependence. The infrared spectrum of pure enstatite contains two main peaks, but several additional peaks are present in Al-bearing samples. The integrated areas of these additional peaks are correlated with $Al_2O_3$ concentration. Some previous work on enstatite appears to have been affected by $Al_2O_3$ contamination. The solubility of water in forsterite, where the activity of $SiO_2$ is buffered by coexisting enstatite is about 40 ppm in all the samples studied here. The O-H stretching spectra of the forsterite crystals contain, in addition to high frequency peaks at 3,500 and 3,650 $cm^{-1}$, large peaks at 3,160 or 3,230 $cm^{-1}$. These spectra are consistent with those previously published for forsterite grown under conditions of high silica activity (Lemaire et al. 2004).

The distribution of water between end member forsterite and enstatite can be derived from the infrared data. At 1,350°C and 2.0 GPa, the average value of $D_{H_2O}^{en/fo} = 2.75$ is lower than previous estimates in more complex systems but higher than that reported in some natural systems. At 1,100°C and 2.0 GPa, the partition coefficient $D_{H_2O}^{en/fo} = 1.34$ indicates a strong effect of temperature on partitioning and at 1,350°C and 1.0 GPa the measured value of $D_{H_2O}^{en/fo} = 2.47$ suggests a small but significant pressure effect.

**Acknowledgements** We acknowledge the National Environmental Research Council for financial support and Dr. S.L. Kearns for assistance with electron microprobe measurements.

## References

Aubaud C, Hauri EH, Hirschmann MM (2004) Water partition coefficients between nominally anhydrous minerals and basaltic melts. J Geophys Res 31:L20611 DOI: 20610.21029/22004GL021341

Bai Q, Kohlstedt DL (1993) Effects of chemical environment on the solubility and incorporation mechanism for hydrogen in olivine. Phys Chem Miner 19:460–471

Bell DR, Ihinger PD, Rossman GR (1995) Quantitative analysis of trace OH in garnet and pyroxenes. Am Mineral 80:465–474

Bell DR, Rossman GR, Maldener J, Endisch D, Rauch F (2003) Hydroxide in olivine: a quantitative determination of the absolute amount and calibration of the IR spectrum. J Geophys Res 108(B2):2105

Bell DR, Rossman GR, Moore RO (2004) Abundance and partitioning of OH in a high pressure magmatic system: megacrysts from the Monastery Kimberlite, South Africa. J Petrol 45(8):1539–1564

Berry AJ, Hermann J, O'Neill H, St.C., Foran GJ (2005) The incorporation of water in mantle olivine. Geology 33(11):869–872

Braithwaite JS, Wright KV, Catlow CRA (2003) A theoretical study of the energetics and IR frequencies of hydroxyl defects in forsterite. J Geophys Res 108(B6):1–9

Brodholt JP (1997) Ab initio calculations on point defects in forsterite ($Mg_2SiO_4$) and implications for diffusion and creep. Am Mineral 82:1049–1053

Dobson PF, Skogby H, Rossman GR (1995) Water in bonninite glass and coexisting orthopyroxene: concentration and partitioning. Contrib Mineral Petrol 118:414–419

Grant KJ, Kohn SC, Brooker RA (2004) Hydrogen partitioning between synthetic olivine, orthopyroxene and melt. Geochim Cosmochim Acta 68:A34

Hirth G, Kohlstedt DL (1996) Water in the oceanic upper mantle: implications for rheology, melt extraction and the evolution of the lithosphere. Earth Planet Sci Lett 144:93–108

Ingrin J, Skogby H (2000) Hydrogen in nominally anhydrous upper-mantle minerals: concentration levels and implications. Eur J Mineral 12:543–570

Inoue T (1994) Effect of water on melting phase relations and melt composition in the system $Mg_2SiO_4$-$MgSiO_3$-$H_2O$ up to 15 GPa. Phys Earth Planet Inter 85:237–263

Koga K, Hauri E, Hirschmann M, Bell DR (2003) Hydrogen concentration analyses using SIMS and FTIR: comparison and calibration for nominally anhydrous minerals. Geochem Geophys Geosyst 4(2):1019 DOI:1010.1029/2002GC00378

Kohlstedt DL, Keppler H, Rubie DC (1996) Solubility of water in the $\alpha$-phase, $\beta$-phase and $\gamma$-phase of (Mg,Fe)2SiO4. Contrib Mineral Petrol 123:345–357

Kohn SC (1996) Solubility of $H_2O$ in nominally anhydrous mantle minerals using 1H MAS NMR. Am Mineral 81:1523–1526

Lemaire C, Kohn SC, Brooker RA (2004) The effect of silica activity on the incorporation mechanisms of water in synthetic forsterite: a polarised infrared spectroscopic study. Contrib Mineral Petrol 147:48–57

Libowitzky E, Beran A (2004) IR spectroscopic characterisation of hydrous species in minerals. In: Beran A, Libowitzky E (eds) Spectroscopic methods in mineralogy, vol. 6. European Mineralogical Union, Budapest, pp 227–279

Libowitzky E, Rossman GR (1997) An IR absorption calibration for water in minerals. Am Mineral 82:1111–1115

Mackwell SJ, Kohlstedt DL (1990) Diffusion of hydrogen in olivine: implications for water in the mantle. J Geophys Res 95:11319–11333

Matveev S, O'Neill H, ST C, Ballhaus C, Taylor WR, Green DH (2001) Effect of silica activity on OH- IR spectra of olivine: Implications for low-$\alpha SiO_2$ mantle metasomatism. J Petrol 42(4):721–729

Matveev S, Portnyagin M, Ballhaus C, Brooker RA, Geiger CA (2005) FTIR spectrum of phenocryst olivine as an indicator of silica saturation in magmas. J Petrol 46(3):603–614

McDade P, Wood B, Van Westrenen WBR, Gudmundsson G, Soulard H, Najorka J, Blundy J (2002) Pressure corrections for a selection of piston-cylinder assembles. Mineral Mag 66:1021–1028

Mierdel K, Keppler H (2004) The temperature dependence of water solubility in enstatite. Contrib Mineral Petrol 148(3):305–311

Paterson MS (1982) The determination of hydroxyl by infrared absorption in quartz, silicate glasses and similar materials. Bull Minérallogie 105:20–29

Peslier AH, Luhr JF, Post J (2002) Low water contents in pyroxenes from spinel-peridotites of the oxidized, sub-arc mantle wedge. Earth Planet Sci Lett 201:69–86

Rauch M, Keppler H (2002) Water solubility in orthopyroxene. Contrib Mineral Petrol 143:525–536

Stalder R (2004) Influence of Fe, Cr and Al on hydrogen incorporation in orthopyroxene. Eur J Mineral 16:703–711

Stalder R, Skogby H (2002) Hydrogen incorporation in enstatite. Eur J Mineral 14:1139–1144